Sensitivity Analysis and Gradient-based Optimisation of Feed Spacer Shape in Reverse Osmosis Membrane Processes Using Discrete Adjoint Approach

Yang Wang[1], Wei He[2,*], Jens-Dominik Müller[1]

1 School of Engineering and Material Science, Queen Mary University of London, London, UK

2 Department of Mechanical Engineering, Massachusetts Institute of Technology, Cambridge, USA

Abstract

Spacers play a significant role in enhancing water permeation in membrane desalination processes but also increase pressure drop and specific energy consumption for freshwater production. The complex coupling of nonlinear channel flow along with mass transfer of water and salts across the membrane makes it challenging to determine an optimal spacer design. Conventional methods employ a design loop based on manual design and re-evaluation, which is time-consuming and typically will only find an improved, but not an optimal design. This paper presents an alternative approach that employs gradient-based adjoint method to explore an optimal design in complex shapes with many design parameters. The novel design methodology provides an effective tool for designers to pursue advanced spacer designs. To elucidate the design method with sensitivities, the spacer in cavity, submerged and zigzag configurations are first analysed with the computed gradients of pressure loss and flow permeation with respect to the displacement of the grid nodes on spacer surface. Then, an optimisation case of cylinder spacers in the zigzag configuration finds an optimal spacer that has 24% pressure loss reduction and only 0.43% permeation drop as compared to a standard cylinder spacer, indicating the new method's potential in finding high-performance spacer designs.

Keywords

Spacer shape optimisation, sensitivity analysis, gradient-based design procedure, discrete adjoint method

* Corresponding author: whe@mit.edu

1. Introduction:

Water scarcity affects approximately one-third of the world populations [1]. Desalination is a viable approach to expand drinking water supplies. Reverse osmosis (RO) is the most widely employed water desalination technology in recent decades. In 2009, RO already accounted for 59% of installed capacity of desalination [2]. Spacers in membrane channels are critical functional components which have been extensively utilised in spiral wound membrane (SWM) modules. In general, spacers improve water permeation across the membrane by increasing shear stress along the boundary layers at the membrane surface, and enhancing flow disturbance to mitigate concentration polarisation (CP). However, spacers in the channels also result in pressure losses. Therefore, the design of spacers is challenging because of: a) the coupled effects between the nonlinear feed flow and the complex mass transfer of both water and salts across the membrane; and b) the trade-off relationship between flow permeation and pressure drop.

Investigations in the past decade have pointed out several typical designs of spacers and analysed their effects on the performance of membrane modules. Ahmad et al. indicate that filaments with triangular cross-section shape had the biggest ability to reduce CP effect, and circular ones caused the lowest pressure drop [3]. Thus, they suggest to use triangular shapes to flows at low Reynolds numbers and circular ones at high Reynolds numbers. Guillen and Hoek study feed spacer shapes in nano filtration (NF) and RO processes, simulate and compare several circular and non-circular spacers [4]. They find that the mass transfer performance is marginally affected by the spacer's shape, but thinner spacers that are spread further apart significantly reduce pressure drop [4]. Amokrane et al. compare elliptic and oval spacer designs, and conclude that those geometries had lower pressure drop compared to conventional ones. Besides, tilted oval spacers mitigate fouling due to the flow structure change in the vicinity of spacers [5]. Concave surfaces diminish pressure drop compared to commercial convex-surface spacers [6]. Experiments also verified that the concave spacers can provide high wall shear rates per unit mass of energy dissipation rate [7]. A novel saw-tooth flow permeation promoter was designed to improve the mixing and back-transport in a flat-sheet membrane module. The experimental results [8] indicate that theses saw-tooth spacers increase the permeation rate by 115.7%-258.0% and reduced the specific energy consumption of larger than 33.8%.

However, most existing studies use a manual design process by carrying out a number of specific pre-defined experiments or/and numerical computations, and are hence time-consuming. As only a finite number of design variants can be evaluated, the resulting shape may be far from optimal. Additionally, this ‘try and compare’ design loop is not suited to explore the designs of irregular, non-periodic and complex structures, which might be inconceivable before. The resulting shapes are very dependent on the experience of operators. Different from conventional manufacturing techniques such as vacuum foaming or extrusion, emerging advanced manufacturing technologies, such as 3D printing offer an opportunity for novel designs, which enable to conceive and manufacture complex shapes and non-recurring patterns [9]. However, the engineer controlling a manual design loop may not have enough ‘out of the box’ thinking for a design that takes advantage of new materials and manufacturing techniques.

To overcome the limitations of a manual redesign process, this study proposes a new design loop using goal-based optimisation with gradient-based methods and gradient evaluation by the discrete adjoint method. The novelties of this paper are to calculate the surface sensitivities of spacer shapes in RO flow channels and to efficiently optimise the spacer shapes based on the surface sensitivities with respect to a predefined objective function, neither of which have been performed in the past for spacer design. Compared to stochastic algorithms such as genetic algorithm and evolutionary algorithms, the use of gradient-based methods enables a significantly decreased number of evaluations during the optimisation.

The primary challenge of using gradient-based algorithms is to quickly and accurately compute the sensitivities of multiple design parameters with respect to the cost function. Simplistic approaches based on finite-differencing are affected by truncation and round-off errors and have a cost that scales with the number of design variables, making this approach prohibitively expensive for optimisation of shapes with complex parametrisation. Tangent linearization or the complex variable approach [10] are able to compute accurate gradients but incur the same computational cost. The adjoint approach, on the other hand, allows computing accurate derivatives at constant cost. This is achieved by solving the adjoint equations, a linearized system of flow equations that propagated infinitesimal perturbations backwards through the model. The exact sensitivities of all the design variables can hence be obtained from a single evaluation of the flow equations and a single evaluation of the adjoint equations, instead of numerous optimisation iterations in which the flow equations are solved at every iteration while using conventional 'try and compare' or stochastic algorithms.

Prior work developed by Seungae et al. successfully proves the efficient goal-based design procedure by applying the continuous adjoint to designing spacers and the flow channel topology in a RO membrane channel [11]. In the continuous adjoint approach, the equations are linearized, transposed and then discretised, which induces a different truncation error computed to the flow discretization. This may lead to issues with convergence of the adjoint system, but most importantly leads to an inconsistency between the zero-gradient predicted by the adjoint and the minimum given by the flow solver. Here we propose to use the discrete adjoint, which proceeds by exactly linearizing the discretised flow equations, the 'primal', and then transposing the system matrix. The discrete approach guarantees that the adjoint and flow discretizations are consistent with the same stationary points. The adjoint also is guaranteed to inherit the linear stability properties of the primal. Most importantly, the discrete adjoint system can be built via Automatic Differentiation (AD), which makes the development and maintenance of adjoint codes feasible.

Therefore, to lay a stepping stone for the gradient-based optimisation of spacers in membrane processes, and efficient spacer surface sensitivities calculation, this paper specifically filled the gap between the RO membrane process and the discrete adjoint method. The significance of this study is to derive the discrete adjoint optimisation solver which is constrained by the CFD system that describes the flow in RO membrane channels. With the developed methodology, this work carried out a sensitivity analysis of spacer shape in a number of spacer orientations. Therefore, the paper is organised as follows. Section 2 introduces the governing equations of flow and mass transfer in RO membrane processes and derives its discrete adjoint. Section 3 presents the validation of the flow and adjoint models using benchmark data. A sensitivity analysis of the spacer shape with respect to permeation rate and pressure loss is carried out in Section 4. This work considers three orientations of transverse spacers, the zigzag, the submerged, and the cavity. The gradient fields of spacer shape are analysed and discussed. Finally, a case study of the gradient-based optimisation loop is illustrated. The shape of the zigzag spacer is optimised by the discrete adjoint gradient to minimise the pressure loss. The obtained optimal spacer shape is analysed and discussed.

2. Problem description and methodology

This section introduces the spacer shape problem considered in this paper, and derives the governing equations for flow adjoint sensitivity in RO membrane channels.

2.1. Geometry of RO membrane channel

We consider here a geometry of a ladder-type spacer (also called a parallel spacer) filled flow channel. The literature proposes diamond-type spacers, and they are not considered in this paper. While the methodology we propose is applicable to any type of geometry. We focus here on conventional cylinder-

type spacers as their smoother geometry permits larger displacements before mesh quality deteriorates. At low Reynolds numbers, the simplification of 2D channel flow assumption is acceptable in the transvers direction. Schwinge et al. defined three types of spacer configuration [12], namely zigzag, cavity and submerged. Since the longitude changing effect is negligible, this work considers the cross-section 2D flow channels with different spacer configurations at the early stage of spacer shape optimisation with sensitivities. In this paper, the flow channels investigated are shown in Figure 1, which illustrate (a) open channel, (b) submerged configuration, (c) cavity and (d) zigzag configurations. Six filaments are our choice to study the different periodicity among these configurations. The flow channel has length L=86.5mm and height H=2mm. The spacer diameter is d=1mm, and interval distance is l_d=8mm [13].

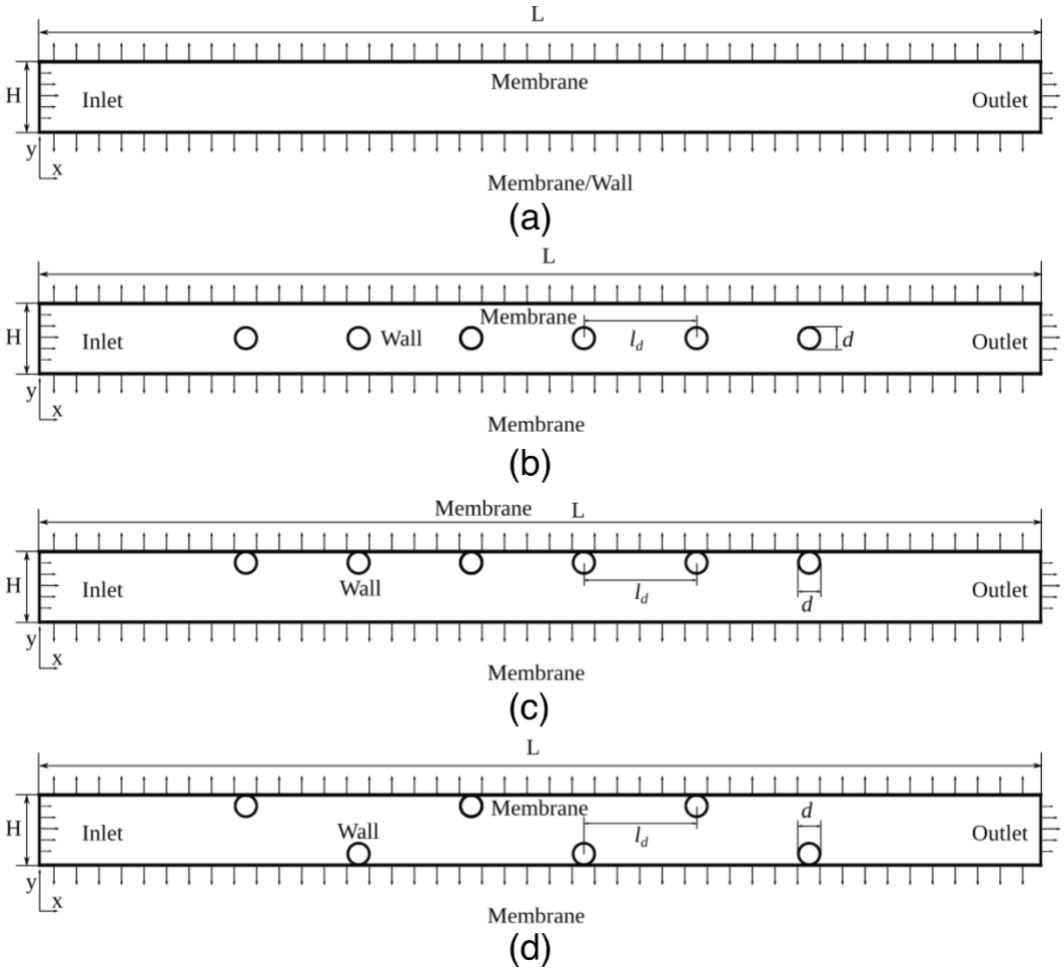

Figure 1 The flow channel considered in this study which represents a typical spacer-filled feed channel in a SWM module: (a) open channel, (b) submerged, (c) cavity, and (d) zigzag spacers configuration.

2.2. Governing equations of RO membrane flow

The flow in the membrane channel is assumed to be a steady-state incompressible Newtonian flow. In the membrane channel, the mass transfer leads to the change of solute concentration, and also the change of fluid density and viscosity. However, these changes occurring during the RO operation are small, so the incompressible system assumption still works to solve this weak compressible fluid based on Boussinesq approximation [14]. The gravity force is ignored because the channel height is low and the gravity difference is small. Therefore, the governing equations of the steady-state RO process are

$$\nabla \cdot (\rho \boldsymbol{u}) = 0 \tag{1}$$

$$\nabla \cdot (\rho \boldsymbol{u}\boldsymbol{u}) = -\nabla p + \nabla \cdot [\mu(\nabla \boldsymbol{u} + \nabla \boldsymbol{u}^T)] \tag{2}$$

The solute transportation satisfies concentration conservation

$$\nabla \cdot (\rho \boldsymbol{u} C) = \nabla \cdot (\rho D \nabla C) \tag{3}$$

where $\boldsymbol{u}$ is the flow velocity (m/s); p is the static pressure (Pa); C is the solution concentration (kg/kg). The viscosity μ (Pa·s), density ρ (kg/m^3), solute diffusion coefficient D (m^2/s) and the solution's osmotic pressure π (Pa) are varied with respect to the solute concentrations. In this study, both the solutions of draw and feed are assumed to be binary mixture of water and NaCl. The variation of these four parameters due to changes in the solute concentration were estimated by the functions presented by Equation (4-7), which are correlated empirically for the physical properties of a NaCl solution at 25 °C [15, 16]

$$\rho = (997.1 + 694C)\ \mathrm{kg/m^3} \tag{4}$$

$$\mu = 0.89 \times 10^{-3}(1 + 1.63C)\ \mathrm{Pa \cdot s} \tag{5}$$

$$D = \max(1.61 \times 10^{-9}(1 - 14C), 1.45 \times 10^{-9})\ \mathrm{m^2/s} \tag{6}$$

$$\pi = 0.805 \times 10^{8} C\ \mathrm{Pa} \tag{7}$$

This study does not resolve the flow inside the membrane [16]. The membrane is hence considered as a two-dimensional plane. The membrane surface is assumed to be smooth and its roughness is not considered. Therefore, the water flux J_w can be expressed as:

$$J_w = K(\delta p - \delta \pi) \tag{8}$$

where J_w equals to the flow normal velocity at the membrane boundary. The water permeability coefficient K is determined by the membrane properties.

To solve the governing equations (1-3), boundary conditions are needed, which are lists in Table 1. The osmosis coefficient C_{os}=0.805×10^8 comes from Equation (7). The concentration boundary condition can be obtained by using the observed rejection coefficient R, which represents a ratio of the rejected solute at the feed side.

Table 1 Boundary conditions for RO CFD model.

Boundary	Boundary condition
Inlet	$\boldsymbol{u} = \boldsymbol{u}_{in}; C = C_{in}$
Outlet	$\partial \boldsymbol{u} / \partial n = 0; \partial C / \partial n = 0$
Non-membrane wall	$\boldsymbol{u} = 0; \partial C / \partial n = 0$
Membrane	$u_t = 0; u_{n,f} = K(\Delta p - C_{os} \Delta C_m); \rho u_{n,f} CR - \rho_f D(\partial C / \partial n)_f = 0$

2.3. Adjoint equations

Gradient-based optimisation algorithms seek to minimise an objective or cost function J by varying a vector of control or design variables $\boldsymbol{\alpha}$. The algorithms find the optimum by searching along a descent direction, first-order gradient-based methods need the first-order gradient $dJ/d\boldsymbol{\alpha}$. In this study, the mesh coordinates of nodes on the surface of the spacer are the design variables. The optimisation problem is described as

$$\min \quad J(\boldsymbol{W}(\boldsymbol{\alpha}),\boldsymbol{\alpha}) \tag{9}$$

subject to the constraint of flow state equation

$$\boldsymbol{R}(\boldsymbol{W}(\boldsymbol{\alpha}),\boldsymbol{\alpha}) = 0 \tag{10}$$

where $\boldsymbol{W}$ is flow state variable vector (e.g. velocity, pressure, and concentration fraction). The constraint in this study, Equation (10), is the residual $\boldsymbol{R}$ of the Navier-Stokes equations (1-2) and the solute transportation Equation (3).

The finite difference (FD) method can be used to calculate the gradient simply, which is

$$\frac{dJ}{d\boldsymbol{\alpha}} \approx \frac{J((\boldsymbol{W}+\delta\boldsymbol{W}),(\boldsymbol{\alpha}+\delta\boldsymbol{\alpha})) - J(\boldsymbol{W},\boldsymbol{\alpha})}{\delta\boldsymbol{\alpha}} \tag{11}$$

where $\delta\boldsymbol{\alpha}$ is a perturbation in control variables and $\delta\boldsymbol{W}$ are the flow state perturbation. Normally, the shape optimisation problems have a much smaller number of objective functions than the number of design variables, like massive mesh points. In the finite-difference approach, one needs to perturb each of the m design variables to get one component in the gradient vector, so the final gradient requires m times computation of perturbed flow solutions:

$$\begin{aligned}
&\frac{dJ}{d\alpha_1} \approx \frac{J((\boldsymbol{W}+\delta\boldsymbol{W}_1),(\alpha_1+\delta\alpha_1)) - J(\boldsymbol{W},\boldsymbol{\alpha})}{\delta\alpha_1};\\
&\frac{dJ}{d\alpha_2} \approx \frac{J((\boldsymbol{W}+\delta\boldsymbol{W}_2),(\alpha_2+\delta\alpha_2)) - J(\boldsymbol{W},\boldsymbol{\alpha})}{\delta\alpha_2};\\
&\qquad\qquad \cdots\\
&\frac{dJ}{d\alpha_m} \approx \frac{J((\boldsymbol{W}+\delta\boldsymbol{W}_m),(\alpha_m+\delta\alpha_m)) - J(\boldsymbol{W},\boldsymbol{\alpha})}{\delta\alpha_m}
\end{aligned} \tag{12}$$

Therefore, this finite-difference method not only evaluates the cost function $J_i = J_i((\boldsymbol{W}+\delta\boldsymbol{W}_i),(\alpha_i+\delta\alpha_i))$ but also computes the perturbed flow $(\boldsymbol{W}+\delta\boldsymbol{W}_i)$ for i=1,2,3, …, m**.** Flow equations $\boldsymbol{R}\big((\boldsymbol{W}+\delta\boldsymbol{W}_i),(\alpha_i+\delta\alpha_i)\big)=0$ are computed m times to obtain the FD gradient. In order to reduce the computational cost of the optimisation in a design problem with a large number of design variables, the adjoint method is used instead. Using the chain rule, the sensitivity can be written as

$$\frac{dJ}{d\boldsymbol{\alpha}} = \frac{\partial J}{\partial\boldsymbol{\alpha}} + \frac{\partial J}{\partial\boldsymbol{W}}\frac{\partial\boldsymbol{W}}{\partial\boldsymbol{\alpha}} = \frac{\partial J}{\partial\boldsymbol{\alpha}} + \boldsymbol{g}^T\boldsymbol{U} \tag{13}$$

where $\boldsymbol{g}^T = \dfrac{\partial J}{\partial\boldsymbol{W}}$ and $\boldsymbol{U} = -\dfrac{\partial\boldsymbol{W}}{\partial\boldsymbol{\alpha}}$. The perturbation matrix $\boldsymbol{U}$ using given information, differentiation and linearization of the state constraint leads to

$$\frac{\partial \boldsymbol{R}}{\partial \boldsymbol{W}}\frac{\partial \boldsymbol{W}}{\partial \boldsymbol{\alpha}}+\frac{\partial \boldsymbol{R}}{\partial \boldsymbol{\alpha}}=0. \tag{14}$$

The flow equation above can also be written as

$$\boldsymbol{AU}=\boldsymbol{f} \tag{15}$$

where $\boldsymbol{A}=\partial \boldsymbol{R}/\partial \boldsymbol{W}$ is the flow Jacobian and the right-hand side is $\boldsymbol{f}$ = -$\partial \boldsymbol{R}/\partial \boldsymbol{\alpha}$. For a unique and convergent solution we can assume that the Jacobian is invertible, and thus $\boldsymbol{U}=\boldsymbol{A}^{-1}\boldsymbol{f}$. Introducing $\boldsymbol{U}$ back in Eq. (13), we can obtain

$$\frac{dJ}{d\boldsymbol{\alpha}}=\frac{\partial J}{\partial \boldsymbol{\alpha}}+\boldsymbol{g}^{T}\boldsymbol{A}^{-1}\boldsymbol{f} \tag{16}$$

Direct computing system equation (15) is very expensive because the right-hand side depends on the design variable $\boldsymbol{\alpha}$, of which there are very many in typical design cases. However, adjoint method does a "conjuring trick" with the last term in Equation (16). By transposing it, we obtain

$$[\boldsymbol{g}^{T}\boldsymbol{A}^{-1}\boldsymbol{f}]^{T}=\boldsymbol{f}^{T}\boldsymbol{A}^{-T}\boldsymbol{g} \tag{17}$$

where the term $\boldsymbol{A}^{-T}\boldsymbol{g}$ is the adjoint variable $\boldsymbol{v}$, or the solution to the adjoint equation

$$\boldsymbol{A}^{T}\boldsymbol{v}=\boldsymbol{g} \tag{18}$$

Here arrives the adjoint equation, whose coefficient matrix equals to the transpose of flow Jacobian. Once the flow converges, flow Jacobian does not change any more, and the adjoint equation is a linear system. Consequently, the final sensitivity is

$$\frac{dJ}{d\boldsymbol{\alpha}}=\frac{\partial J}{\partial \boldsymbol{\alpha}}+\boldsymbol{v}^{T}\boldsymbol{A}\boldsymbol{A}^{-1}\boldsymbol{f}=\frac{\partial J}{\partial \boldsymbol{\alpha}}+\boldsymbol{v}^{T}\boldsymbol{f} \tag{19}$$

The 'Adjoint equivalence' of the tangent-linear and adjoint sensitivities can be shown by

$$\boldsymbol{g}^{T}\boldsymbol{U}=(\boldsymbol{A}^{T}\boldsymbol{v})^{T}\boldsymbol{U}=\boldsymbol{v}^{T}\boldsymbol{A}\boldsymbol{U}=\boldsymbol{v}^{T}\boldsymbol{f} \tag{20}$$

In the discrete approach, automatic differentiation (AD) tools differentiate the conservative fluxes residual $\boldsymbol{R}$ in a reverse mode. In this case, the *Tapenade* AD-tool [17] is used. The flow solver computes a number of sparse matrix vector products of type $(\partial \boldsymbol{R}/\partial \boldsymbol{W})\cdot\boldsymbol{W}$ in a particular block sequence; the adjoint equivalent is achieved by assembling transposed matrix-vector products of the type $(\partial \boldsymbol{R}^{T}/\partial \boldsymbol{W})\cdot\boldsymbol{v}$. The steady flow solution converges with the fixed-point iterations, allowing us to differentiate only the final iteration [18], which improves the computational efficiency. Furthermore, the discrete adjoint solver eliminates the differentiation invariant elements from the solver stack such as linear solvers, and replaced them with appropriately modified calls to the same solver [19]. The transposed Jacobian and same linear solvers calls result in the similar computation cost of adjoint equation compared with its primal.

2.4. Gradient-based optimisation using the discrete adjoint method

The in-house code GPDE [19] has been developed specifically to support the development of a discrete adjoint variant for gradient computation. Figure 2 illustrates the flowchart of the CFD based adjoint

method loop. The design parameters or control variables, e.g. displacement of nodes on the spacer surface, are targeted and labelled in the CAD or mesh geometry at the beginning. CFD solvers compute the flow fields. The sensitivity of the cost function is computed using the discrete adjoint solver. The optimiser, with provided sensitivity, proposes an altered geometry of the shape by updating the design variables to achieve descent, and a new mesh can be produced based on these. The optimisation loop is terminated when the gradient-magnitude has become small enough to accept a near-optimal solution.

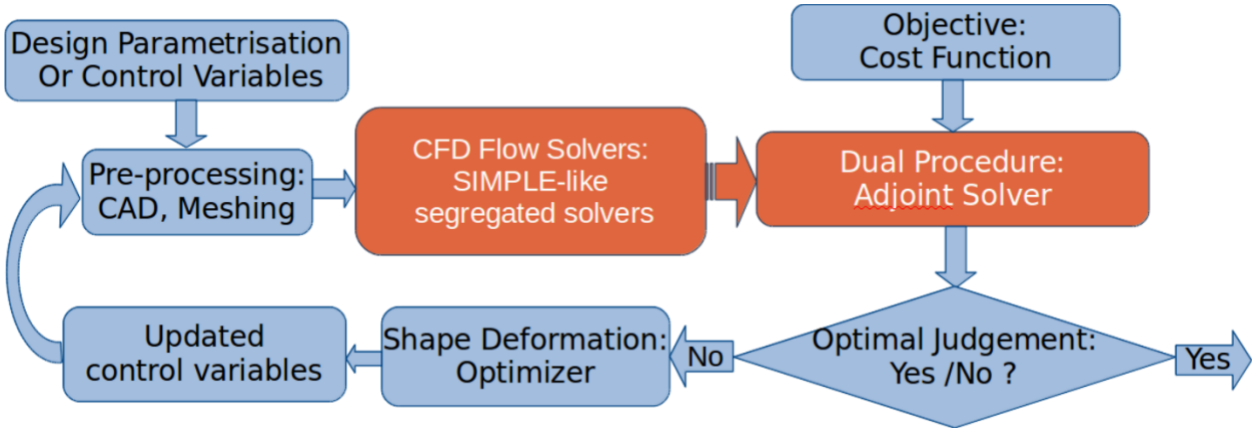

Figure 2 The proposed gradient-based optimal design loop for spacer shape optimisation

In this work, the backtracking line search algorithm along with Armijo-Goldstein condition drives the optimisation iterations [20]. The shape is parametrised on the computational mesh with non-slip wall boundary grid nodes allowed to move in the surface-normal direction. To avoid oscillatory shapes, an explicit smoothing filter is normally applied to the node-based optimisation [21].

3. Validation of the developed CFD constrained adjoint optimisation solver

Before carrying out the computation and spacer shape optimisation in RO membrane flows, the developed CFD solver and adjoint optimisation solver were validated as shown below.

3.1. Validation of the developed CFD flow solver

For 2D channel viscous flow, pressure drop in the channel with two impermeable walls can be evaluated according to Darcy-Weisbach's law for Poiseuille flow [22],

$$\Delta p = (\frac{1}{2}\rho u_{avg}^2)(\frac{24}{\mathrm{Re}})(\frac{x}{h}) \tag{21}$$

where Reynolds number is scaled as $\mathrm{Re} = \rho u_{avg}(4h)/\mu$; h is the half channel height as $2h$=H where H is the channel height; x is the distance from the channel inlet. In a channel with the top and bottom walls being permeable, Berman's solution gives the pressure drop as [23, 24]

$$\Delta p = (\frac{1}{2}\rho u_{avg}^2)(\frac{24}{\mathrm{Re}} - \frac{648}{35}\frac{\mathrm{Re}_w}{\mathrm{Re}})(1 - \frac{2\,\mathrm{Re}_w}{\mathrm{Re}}\frac{x}{h})(\frac{x}{h}) \tag{22}$$

where $\mathrm{Re}_w = \rho u_w h/\mu$ is the local Reynolds number at the permeable wall boundary. The geometric open channel domain has the height H=0.001m and the length L=2m. The inlet average velocity u_{avg} is 0.1m/s. The Reynolds number scaled by the inlet velocity for the channel flow is 200. The fluid has a

density of ρ=1000 kg/m^3 and viscosity of μ=10^{-3} Pa·s. The permeation velocity is taken as constant at 8×10^{-6} m/s. The inlet velocity is assumed to be fully developed. Its distribution expressed as

$$u = 6u_{avg}\frac{y}{h}(1-\frac{y}{h}) \tag{23}$$

where *y* is the vertical distance along *y* direction and *h* is the half of the channel height. The pressure drops along the channel *x* axial direction achieved by Poiseuille's, Berman's and GPDE's solutions are shown in Figure 3.

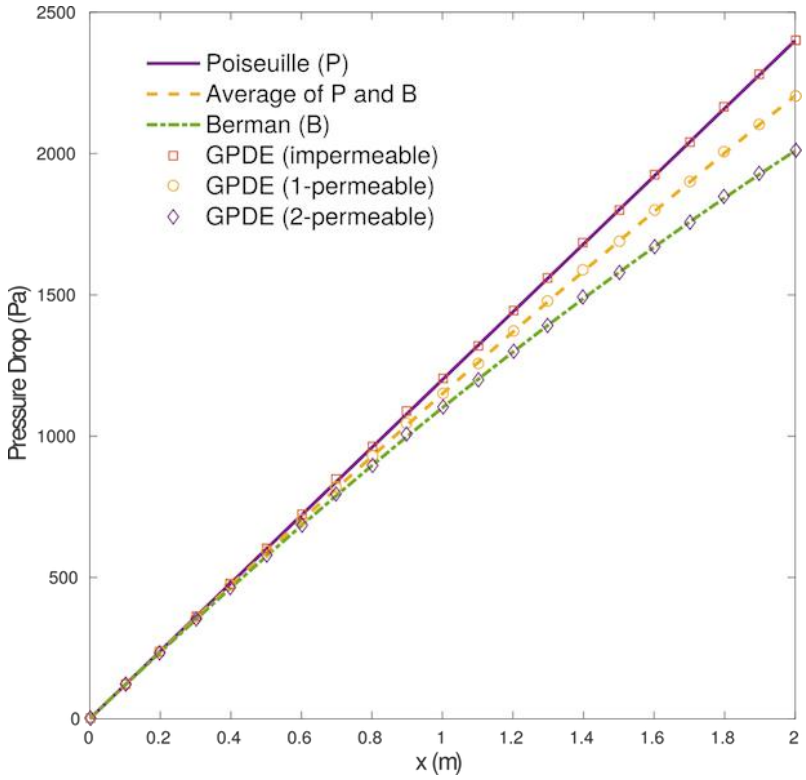

Figure 3 Pressure drops obtained via GPDE's computation and analytical solutions

For a RO membrane process, the solute fraction exerts a large influence on the permeation flux when a constant operational pressure is applied. Normally, feed has a much higher solute fraction in RO membrane processes, which dominates the permeation velocity. Thus, the computation of both feed and draw channels is simplified as a single channel flow in this paper. The solution obtained with GPDE is compared to Fletcher's numerical results [25] as shown in Figure 4. In Figure 5, the membrane permeate flux computed by GPDE is also validated with experimental data [26]. The comparisons show a good agreement between the numerical and experimental benchmarks and GPDE, which validates the GPDE flow solver for a RO model.

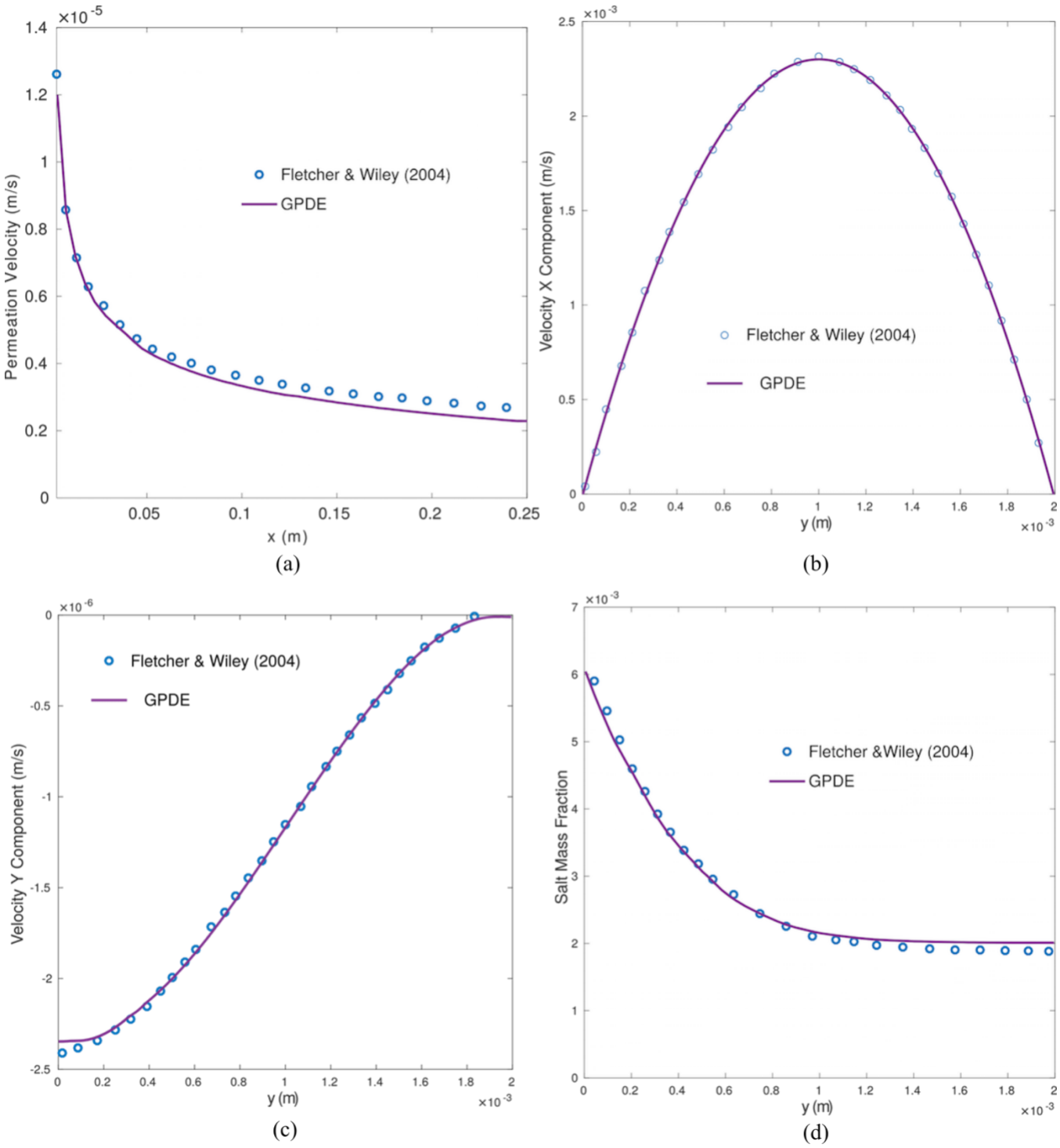

Figure 4 GPDE's results vs. Fletcher's results: (a) permeation velocity profiles along the membrane, (b) velocity x component profiles, (c) velocity y component profiles, and (d) the salt mass fraction profiles along y direction at x=240mm

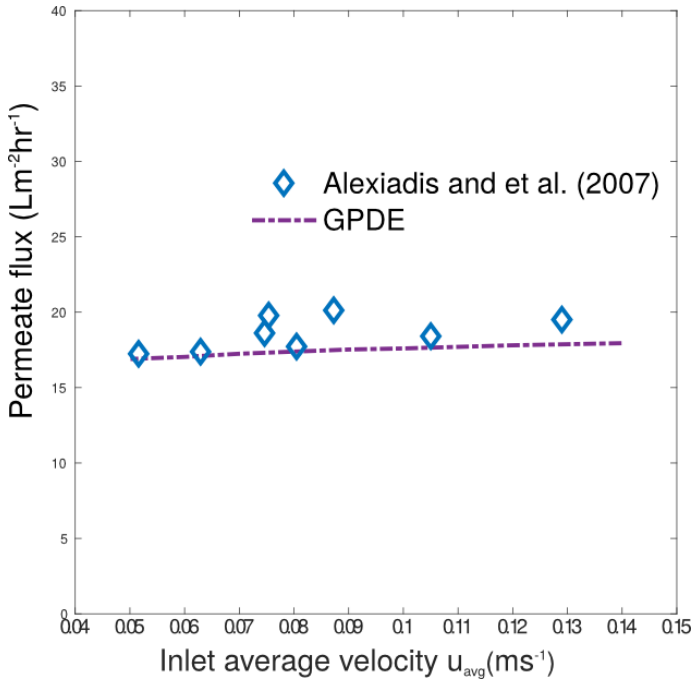

Figure 5 GPDE's permeation rates vs. experimental data.

3.2. Validation of the developed discrete adjoint optimisation solver

A major challenge of the numerical model developed in this study is to drive a discrete adjoint solver for the complex flow and mass transfer in RO membrane channels. Compared to the existing adjoint solvers for the N-S equation based CFD models, an additional convention-diffusion equation, as Equation (18) derived in Section 2.3, with new membrane boundary conditions was incorporated to the N-S equation system. The advantage of using AD [27] is that, once the initial effort of setting up the AD has been done, modification of the source or additional transport equations and flux boundary conditions can be incorporated into the adjoint solver either fully automatically or at least straightforwardly.

In order to verify the accuracy of the developed adjoint solver, the adjoint sensitivities are compared to finite difference approximations and tangent-linear ones. Flow in an open channel as the verification case is shown in Figure 1 (a). One non-slip wall, one permeable membrane, one inlet and one outlet boundary compose four sides of this 2D rectangle computational domain. The inlet velocity distribution imposes a fully-developed profile as shown in Equation (23). The operational pressure is 898.7 kPa and the observed rejection rate is 99.5% for the validation case. The water permeation coefficient of membrane is 6.93×10^{-12} m/(s·Pa) [28]. The salt concentration field is initialized as 0.002 kg/kg. The design variables are the bottom non-slip wall boundary nodes with constraint of moving in surface-normal direction. The objective function for the validation is the average permeation flux. The flow field and the normal sensitivities of the impermeable wall surface are plotted in Figure 6. Sensitivities calculated using three methods are shown in Table 2. If we use tangent linear result as a reference, the smallest absolute difference of FD with step-size $\Delta x = 3.5\times10^{-7}\,\mathrm{m}$ is about $4.5\times10^{-10}\ \mathrm{s}^{-1}$ which is the objective of average permeation rate in m/s per perturbed distance in 1 m, and the discrete adjoint calculated sensitivity whose the minimal absolute difference from all the design variables is about $7.8\times10^{-10}\ \mathrm{s}^{-1}$. Thus the discrete adjoint solver has satisfactory accuracy for calculating the sensitivity field compared to other sensitivity computations.

Table 2 Comparison of sensitivities between different methods.

Method	Sensitivity (1/s)	Difference_{abs} (1/s)
Finite difference	-8.605×10^{-7}	4.455×10^{-10}
Tangent linear	-8.610×10^{-7}	0
Discrete adjoint	-8.610×10^{-7}	7.849×10^{-10}

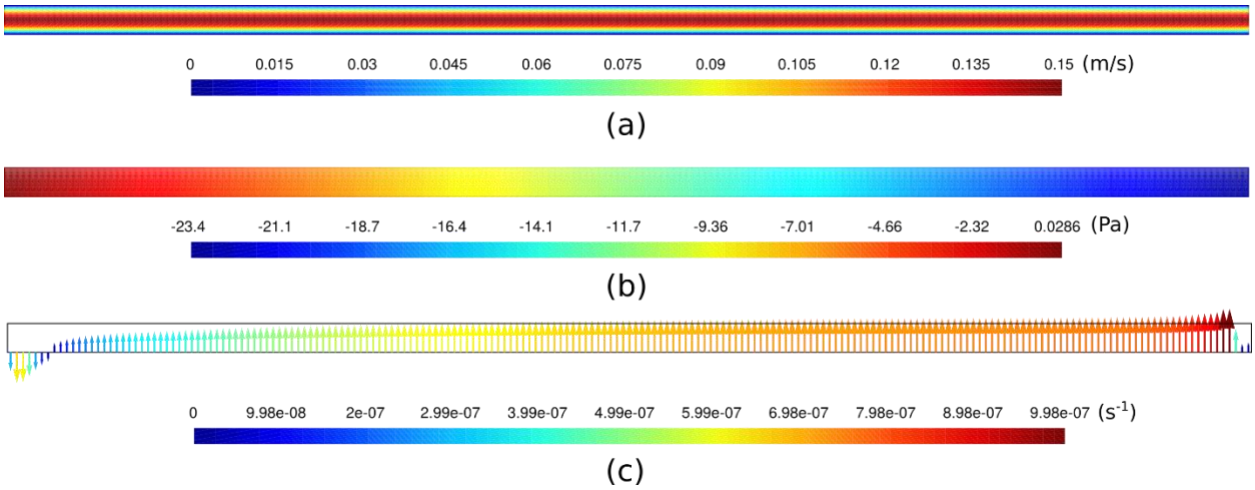

Figure 6 Open channel solutions: (a) velocity magnitude distribution, (b) pressure field, and (c) impermeable wall surface normal sensitivities respect to average permeation flux.

4. Results and discussion

This study considers three spacer configurations, zigzag, submerged and cavity, in the RO membrane channel flow. A boundary-refined non-uniform mesh is generated for all the simulated cases.

4.1. Objective functions in the RO membrane process

Table 3 lists all the objective values among different arrangements with cylinder-shape spacers, where permeate flux and pressure drop are u_n and Δp.

Table 3 Objective function results among different configurations and Re numbers

Configura-tion	Re=44.8		Re=224		Re=448		Re=896	
	$u_n(\text{m/s})$	$\Delta p(\text{Pa})$	$u_n(\text{m/s})$	$\Delta p(\text{Pa})$	$u_n(\text{m/s})$	$\Delta p(\text{Pa})$	$u_n(\text{m/s})$	$\Delta p(\text{Pa})$
Open channel	4.34×10^{-6}	2.27	4.68×10^{-6}	11.52	4.78×10^{-6}	23.08	4.85×10^{-6}	46.20
Cavity	4.62×10^{-6}	4.23	4.88×10^{-6}	29.85	4.94×10^{-6}	74.26	4.99×10^{-6}	187.5
Submerged	4.52×10^{-6}	7.30	4.83×10^{-6}	49.74	4.92×10^{-6}	130.2	4.99×10^{-6}	358.5
Zigzag	4.64×10^{-6}	4.16	4.89×10^{-6}	29.67	4.95×10^{-6}	74.89	5.00×10^{-6}	207.9

The presence of the spacers significantly changes the feed flow in the membrane channel. According to the results, the pressure drop is significantly increased in all the spacer-filled flow channels rather than the one without spacers. The highest pressure drop occurs in the submerged configuration, and pressure drops are similar to each other for the cavity and zigzag configurations.

On the other hand, the permeate flux is similar between the three configurations. Although the zigzag shows a slightly better mass transfer performance when Reynolds number is low, the improved mass transfer becomes insignificant with the increase of Reynolds number, as almost identical pressure drops between the three configurations indicated in Table 3 at Reynolds number of 896. Generally, two mechanisms of transfer enhancement by spacers are: 1) flow separation perpendicular to the bulk flow resulting in the flow re-attachment and re-development along the boundary layer (high CP layer) next to membrane surface behind spacers; 2) high shear stresses to membrane surfaces caused by the increased flow velocity gradients due to spacers. The high shear stress increases the solute diffusion which decreases the polarised salt concentration in the boundary layer.

4.2. Sensitivity analysis using the discrete adjoint method

In this study, the spacer shape, i.e. spacer surface geometry, is discretized through the nodes on the surface, hence the design variables are is the surface-normal displacements of each of the grid nodes representing a spacer. In the simplified 2D spacer geometry, the spacer shape cross-section is a continuous curve. The surface sensitivities (or gradients) assess how the selected objective function will vary if the nodes on ‘the continuous curve’ move in their normal directions. The objective considered for surface sensitivity is either decreasing the pressure drop or increasing the permeation rate.

For the cavity case, the flow field in the spacer-filled channel is shown in Figure 7. The gradients w.r.t. permeation rate and pressure drop are shown respectively in Figure 8 and Figure 9. The third and the fourth filament of the six filaments filled flow channel as illustrated in Figure 1(b) are considered to undertake the sensitivity analysis. This study also selects the third and fourth filaments for sensitivity analysis in the other spacer arrangements. The gradient field is normalized in these figures to indicate the sensitivity distribution.

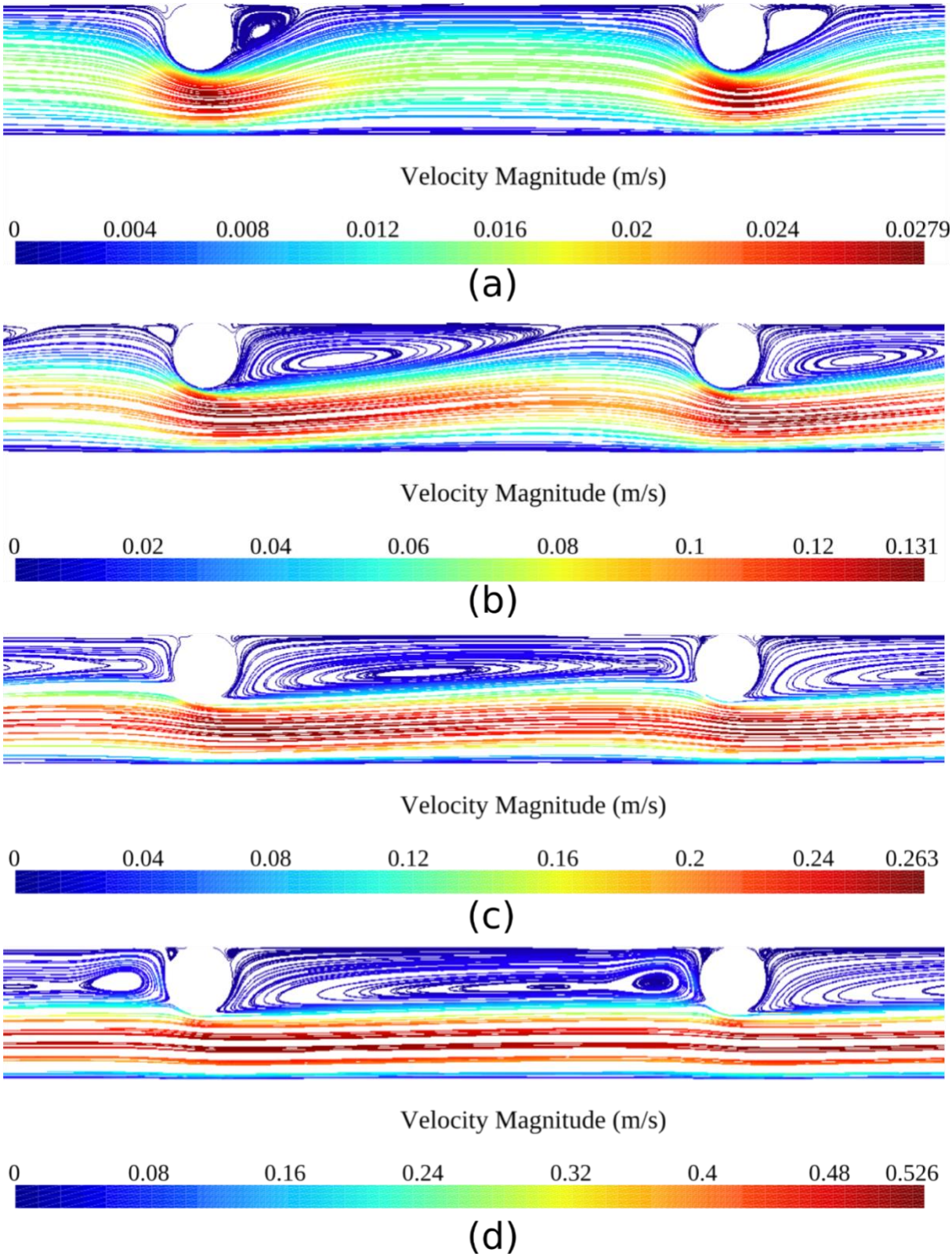

Figure 7 Streamlines of the cavity configuration channel flows at (a) Re=44.8, (b) Re=224, (c) Re=448, and (d) Re=896

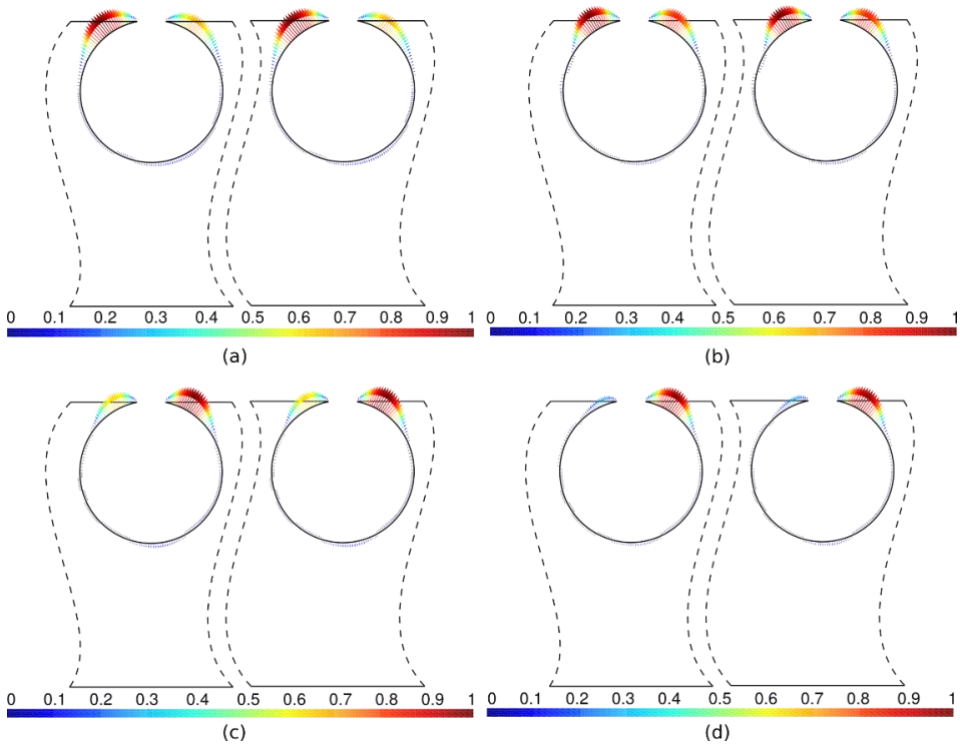

Figure 8 Permeation flux sensitivities of cavity spacers in flows at (a) Re=44.8, (b) Re=224, (c) Re=448, and (d) Re=896. The curved dotted lines indicate the segments of the spacer-filled flow channel.

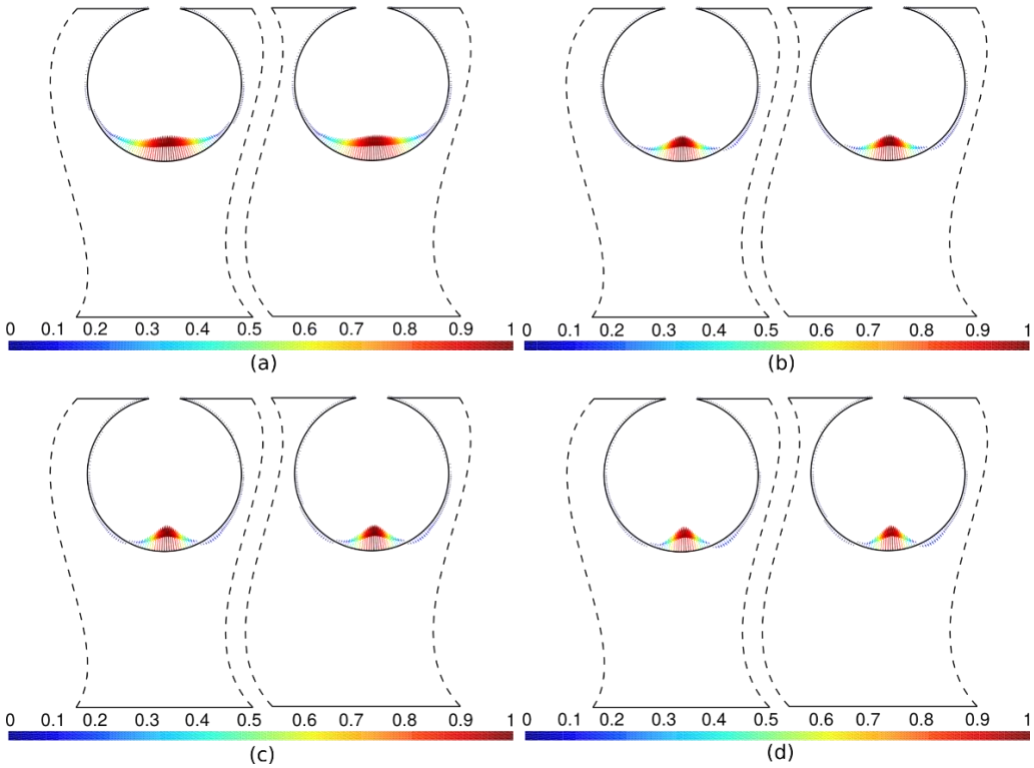

Figure 9 Pressure drop sensitivities of cavity spacers in flows at (a) Re=44.8, (b) Re=224, (c) Re=448, and (d) Re=896

In a cavity spacer configuration, due to the placement of the spacers at the membrane surfaces, the fluid is forced to flow around the spacers where boundary layer is disturbed (compared to the flow in the open channel). The vertical motion in the flow separation area behind the spacers increases the mixing of the solutes in the boundary layer, and hence increases water permeation. The surface sensitivity of the spacer shape w.r.t. permeation flux rate is shown in Figure 8. At all Re, the highest gradient values locate at corners between the filament and the membrane, namely the stagnant zone. There are vortices in this area as shown in Figure 7, either front or behind the filaments. Depending on the Re, the gradient distribution varies. The peak permeation sensitivity is found upstream of the filament in low Re flows, as shown in Figure 8(a) and Figure 8(b), while it is found downstream of the filament in the cases at higher Re as shown in Figure 8(c) and Figure 8(d). Therefore, these sensitivities that adapt to the varying flow fields can enable a flow-customized optimization, where the spacer shape is perturbed in the direction that optimize the objective function in this particular flow condition.

Conversely, the sensitivities related to minimising pressure drop are plotted in Figure 9. The nodes on the filament's lower surface which most protrudes into the channel have the highest pressure drop sensitivities. Unsurprisingly, the shape modification suggested by the gradients, would reduce the blockage in the channel. Flow velocity and drag between spacer tip the opposite wall and thus decrease. Increasing the Reynolds number lets the sensitive regions concentrate at the lower surface apex of spacers. It indicates the apex's role in generating vertex may become relatively more significant when the Reynolds number is high.

The flow field of the submerged configuration is shown in Figure 10. The following Figures 11 and 12 respectively show the gradients w.r.t. permeation rate and pressure drop. For improving the permeation, two distinct areas of high sensitivity are found on the upper and lower filaments. To reduce the pressure drop, the sensitivities indicate almost opposite directions to the ones in Figure 11. Both of Figure 11 and Figure 12 demonstrate that the most sensitive parts are shifted to the surface apex with the increase of the Re. As the submerged spacers are placed in the middle of the channel, the two surfaces of spacers contribute the objectives equally.

According to the flow pattern at low Re shown in Figure 10(a), there is no noticeable flow separation. Figure 11(a) demonstrates that the most sensitive parts at the low Re are the regions in front and behind the apexes of the spacer surfaces for improving permeation. Using the sensitivities to perturb the nodes in their normal direction, one obtains the new spacer shape, which narrows the flow path above and underneath the submerged spacers and prolongs the high-speed region. When Re increasing, the flow separation behind spacers becomes increasingly strengthened as shown in Figure 10(b-d). Spacers with sharper apexes governed by the gradient profile in Figure 9(b-d) will further strengthen the flow separation.

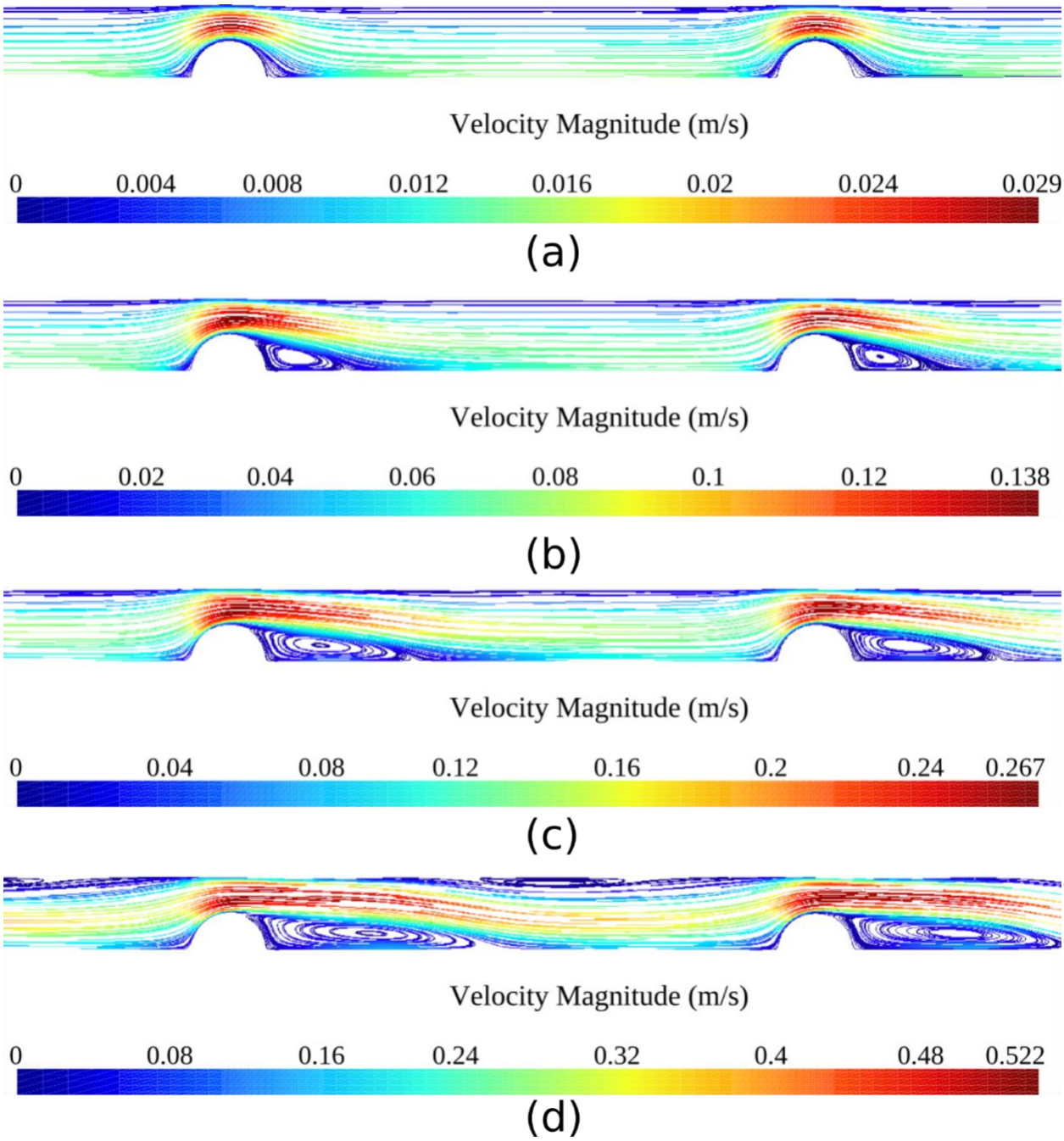

Figure 10 Streamlines of the submerged configuration channel flows at (a) Re=44.8, (b) Re= 224, (c) Re=448, and (d) Re=896

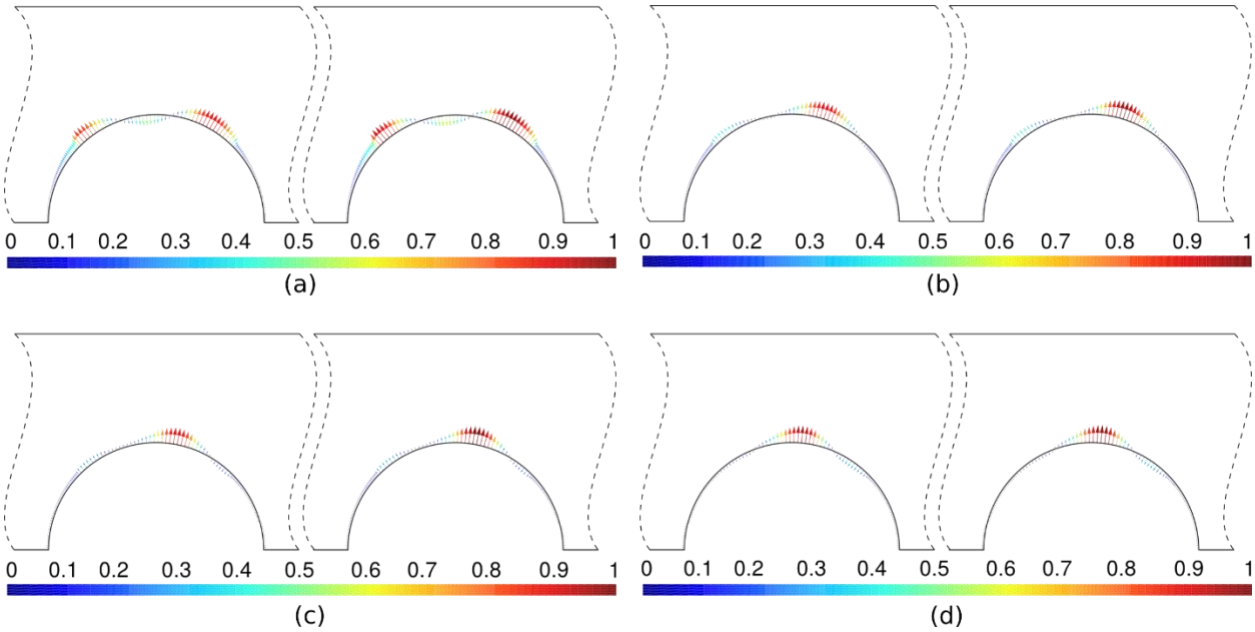

Figure 11 Permeation flux sensitivities of submerged spacers in flows at (a) Re=44.8, (b) Re= 224, (c) Re=448, and (d) Re=896

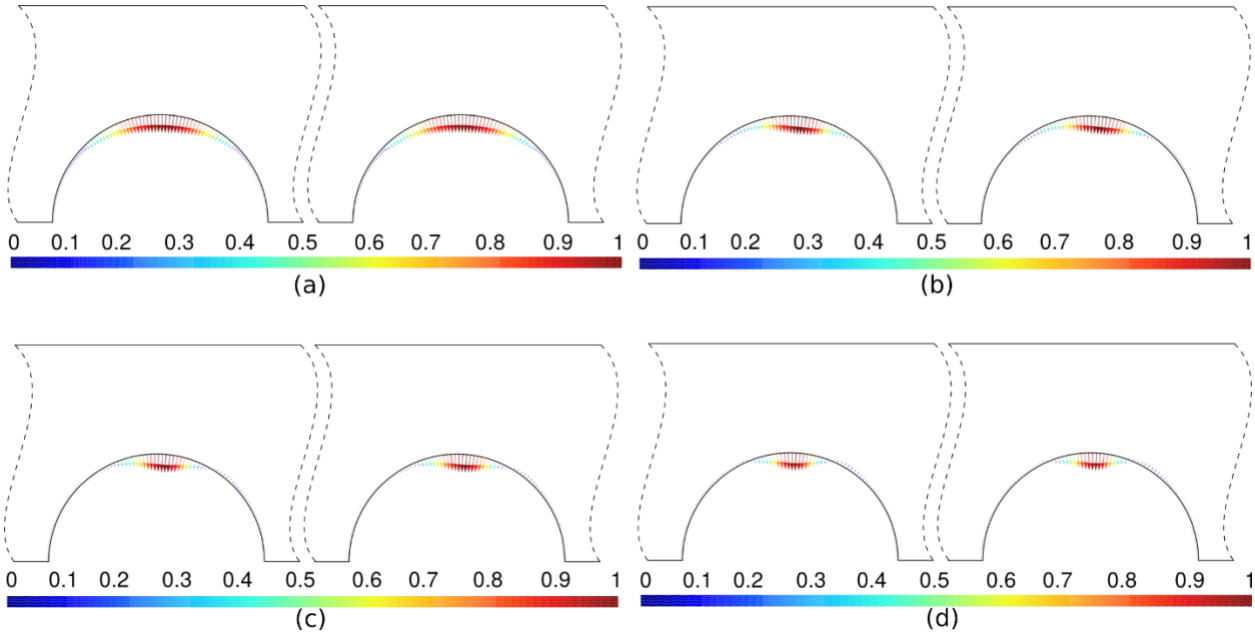

Figure 12 Pressure drop sensitivities of submerged spacers in flows at (a) Re=44.8, (b) Re= 224, (c) Re=448, and (d) Re=896

The streamlines in the zigzag configuration are plotted in Figure 13. The gradient w.r.t. permeation rate and pressure loss are shown in Figure 14 and Figure 15 respectively.

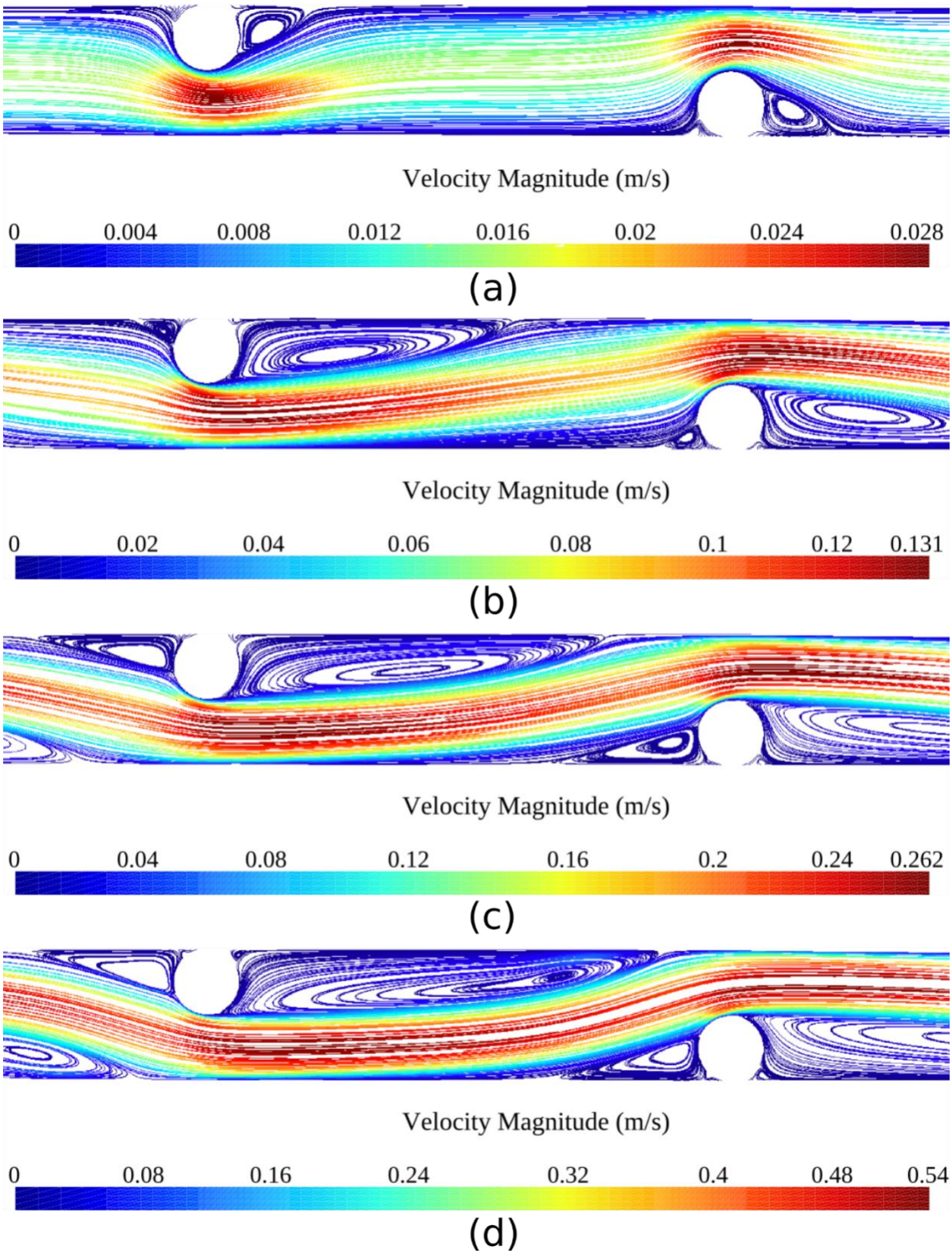

Figure 13 Streamlines of the zigzag configuration channel flows at (a) Re=44.8, (b) Re=224, (c) Re=448, and (d) Re=896

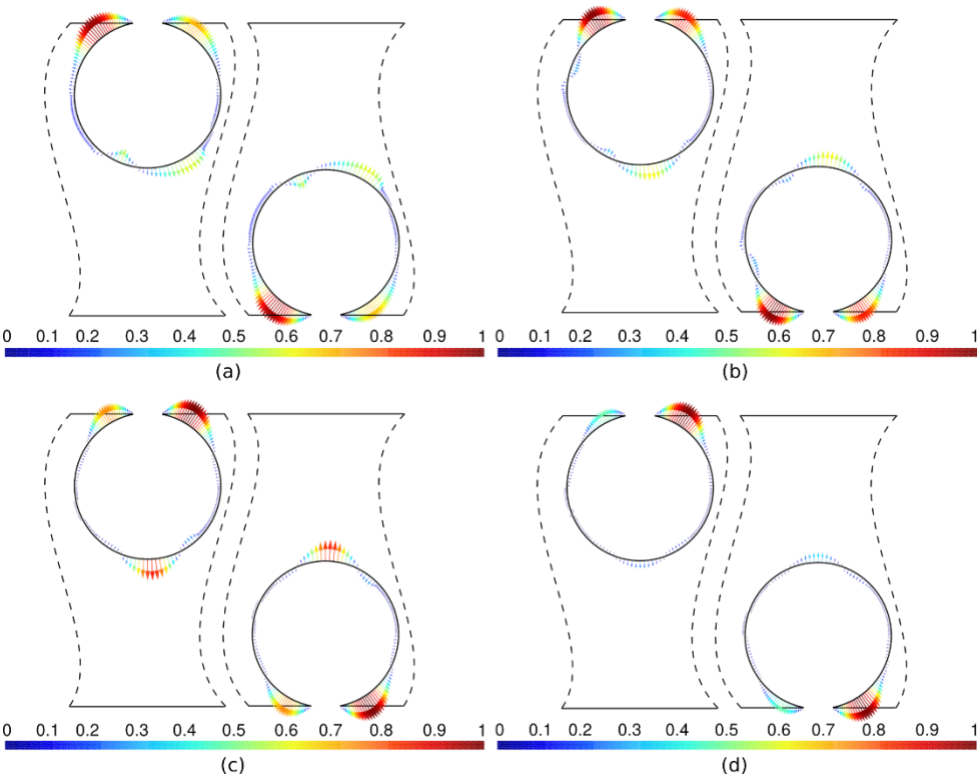

Figure 14 Permeation flex sensitivities of zigzag spacers in flows at (a) Re=44.8, (b) Re= 224, (c) Re=448, and (d) Re=896

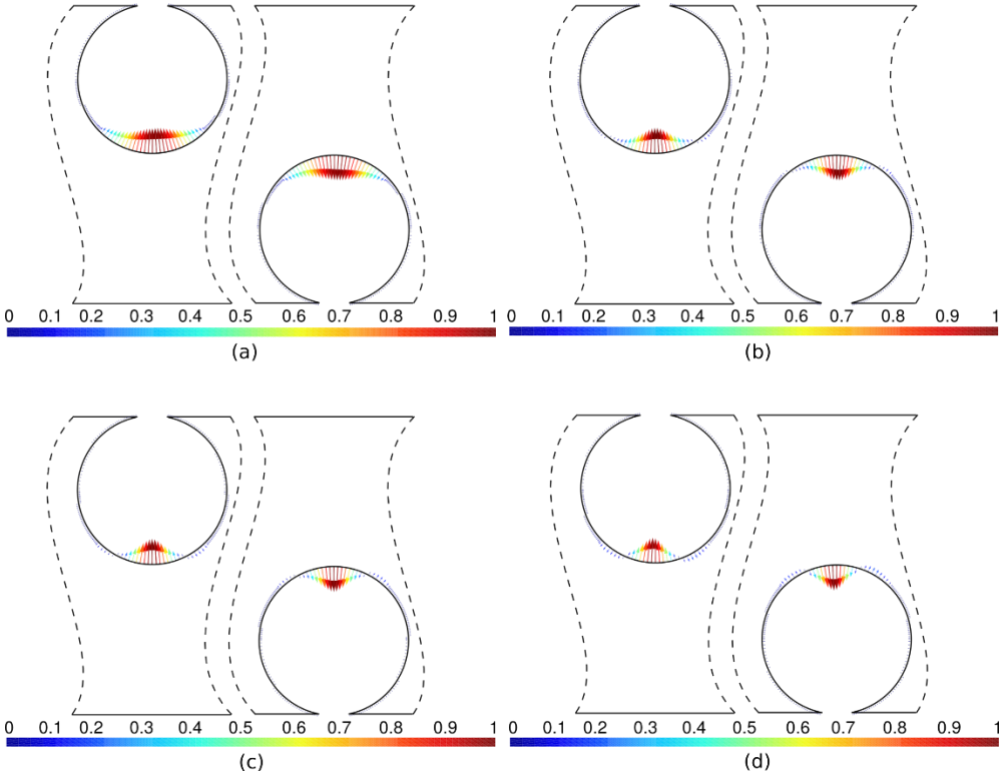

Figure 15 Pressure drop sensitivities of zigzag spacers in flows at (a) Re=44.8, (b) Re= 224, (c) Re=448, and (d) Re=896

In order to maximise flow permeation, areas with high sensitivity move from the front of filaments to the back when Re increasing, which is similar with cavity cases. The gradients in the corners are larger than ones on the upper and lower surfaces as found in Figure 14. However, the sensitive regions on zigzag spacers surfaces are different from both of cavity and submerged arrangements. Not only in the stagnant zones, the larger gradients also appear on both of upper and lower sides of filaments. There are more than one ‘sensitivity peaks' occurring along the spacer surface. These gradient distributions indicate the mass transfer enhancement achieved by the zigzag configuration. The ‘sensitivity peaks’ in the central area will guide the perturbation of spacer shape to the one with sharper apexes, which promotes flow separation and increases the velocity variance. Besides, the ‘sensitivity peaks’ next to the membrane will direct the shape to occupy the corners and decrease the volumes occupied by stagnant zones.

The sensitivities w.r.t. pressure drops in the zigzag configuration show similar trends with ones in the cavity and the submerged configurations. As shown in Figure 15, the most sensitive parts of spacer shape are away from the membrane boundaries. These will guide spacers to be a flattened shape after the gradient-based mesh deformation.

4.3. Spacer shape optimisation in the RO membrane channel

The geometry of the spacers strongly influences pressure loss compared to permeability [4]. The objective function evaluation results in Table 3 indicate that spacer placement in the membrane channel is essential for permeation improvement, but it has a substantial effect on pressure drop. In this context, because the primary focus of this study is to demonstrate the automatic design procedure with sensitivities calculated using the discrete adjoint method, this section carries out a case study of optimisation for minimising pressure drop. As a baseline geometry, we have chosen the zigzag arrangement at Re=44.8. The objective of this optimisation is to reduce the pressure drop by modifying the spacer shape, with a negligible or acceptable permeation reduction compared to that of the baseline geometry. It should be noted that the proposed gradient-based design loop can be used for other spacer shape optimisations with different spacer configurations, Reynolds number, etc.

The shape optimisation adopts steepest descent. A back-tracking line search along with Armijo-Goldstein condition is carried out to safeguard the descent. The original shape, solid line in Figure 16, changes based on the gradient computed via discrete adjoint solver at each optimisation iteration in order to minimise the pressure drop. Both the objective function and the gradient converge during the iterations as shown in Figure 17. The optimised shape is illustrated as the dashed line in Figure 16. Both the objective function and the gradients converge during the optimisation iteration as shown in Figure 17. The optimised spacer shape is a flattened surface toward the channel centreline compared to the traditional cylinder spacers. The pressure drop is reduced by 24%, with a permeating flux decrease by 0.43%.

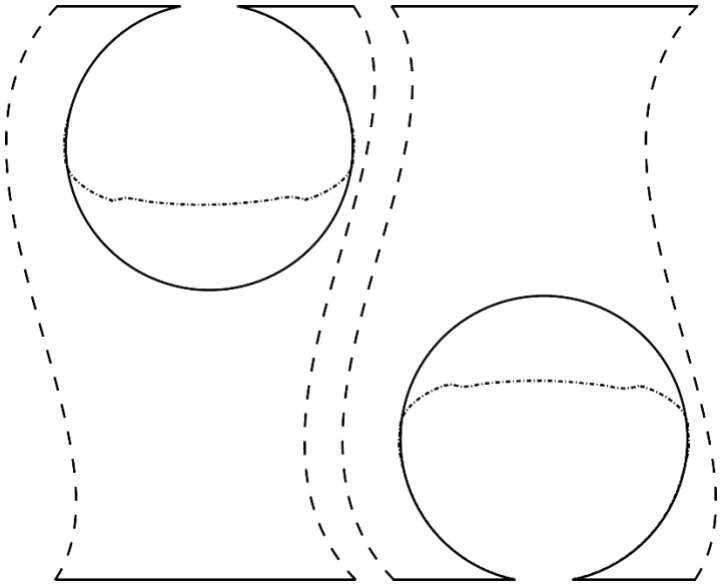

Figure 16 The optimised spacer shape design in the case study

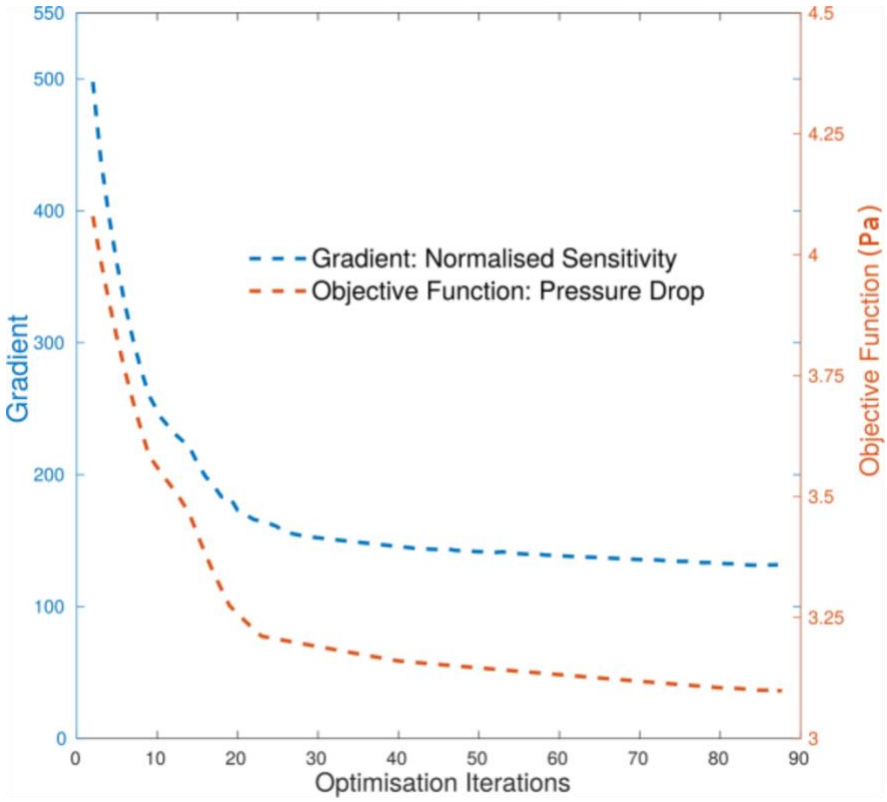

Figure 17 Optimisation convergence curves of gradients and objective function

The comparison of streamlines between the baseline and optimised shapes are plotted in Figure 15. Both computations use the same flow parameters and boundary conditions. The cross-section area open to the flow expands because of the reduced spacer height, which decreases the flow speed in the core region of the main flow. The velocity gradient thus reduces and shear stresses become smaller, which both reduce friction losses which is the main reason for the decrease of pressure drop as there are no significant flow separations in either flows. As shown in Figure 15, there are slightly smaller vortices behind the optimised cylinder compared to the original flow pattern. The flow mixing level does not change dramatically and streamlines next to the membranes remain almost the same, so the permeation reduces only in a small degree.

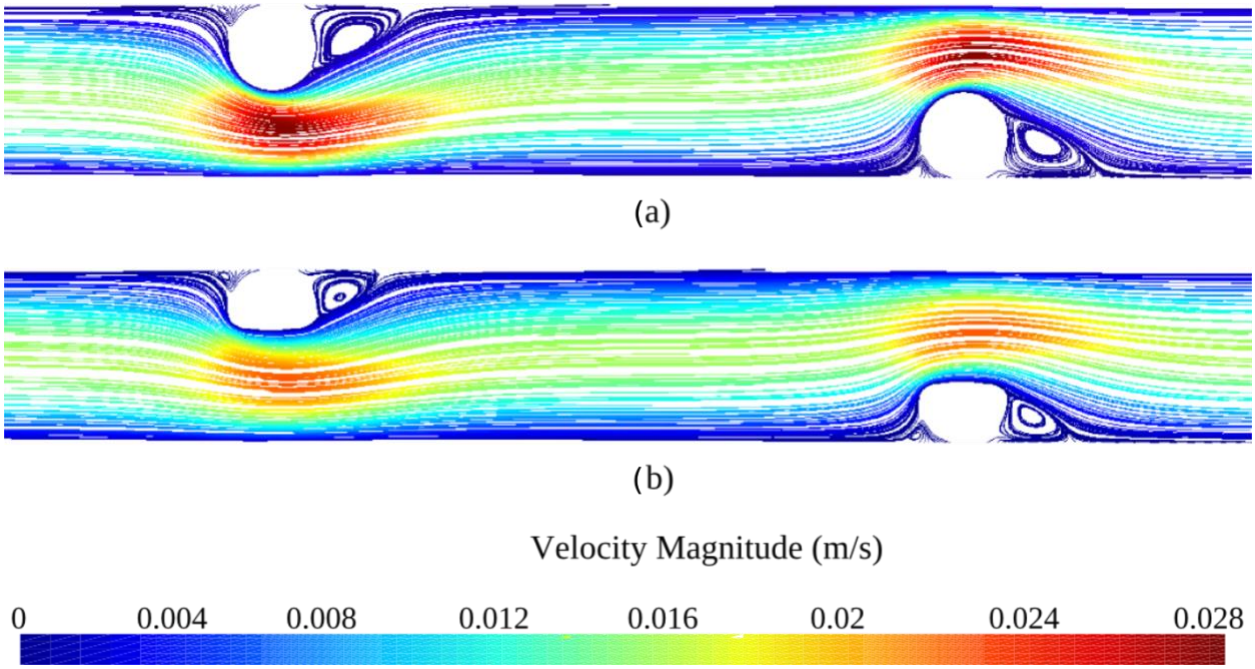

Figure 18 Streamline comparison between flow fields with the original and the optimised spacer shape.

5. Conclusion:

This work applied the discrete adjoint method to perform sensitivity analysis in RO membrane channels. Three types of transverse spacers are considered, namely the cavity, submerged and zigzag configurations. Channel flow patterns and the mechanisms of performance improvements were discussed. A methodology for sensitivity analysis and gradient-based optimisation has been developed, which first uses CFD to compute flow fields and objective functions in RO membrane channels and then applies the discrete adjoint method to calculate the gradient of the objectives w.r.t. design parameters controlling the spacer geometry.

Using this methodology sensitivity analysis was applied to all three configurations to compute the sensitivities of the spacer shape with respect to both permeation flux and pressure drop. In the final step, these sensitivity were used to drive a gradient-based optimisation loop: a case study of minimising pressure drop is carried out in a flow channel with a zigzag spacer configuration. In the channel with the shape-optimised spacers, the pressure drop was reduced by 24% with only 0.43% permeate flux reduction.

The gradient analysis indicates the parts of spacer geometry which affect most significantly to the objective function. Our results confirm that the permeation rate of typical spacer geometries, as studied here, is not very sensitive to shape modifications, as the optimisation barely affects permeation rate. On the other hand, even an optimisation with limited geometric freedom can achieve a significant reduction in pressure loss.

The gradient-based spacer design loop establishes the basis for spacer shape optimisation among different RO channel flows, the case study of the spacer shape optimisation in a zigzag configuration at low Re is a paradigm demonstrating that the methodology works effectively to vary the spacer surface geometry with the discrete adjoint sensitivities through the optimisation iterations. The new thinner and flatter spacer design indicates a significant pressure loss reduction, i.e. pumping power reduction, in RO desalination to produce drinking water at low Re. Therefore, following the developed spacer design loop of this study based on discrete adjoint gradient, the next step is to investigate and optimise the spacer shape in different orientations at various Reynolds numbers, and explore the optimal spacer designs at various flow and membrane conditions. The high-fidelity analysis allows an accurate trade-off between possibly competing objectives in more complex geometries where the shape modification has an effect on both permeation and pressure drop.

The current study was carried out in 2D, which neglects transversal motion in the span-wise plane. That motion however can be very powerful in enhancing mixing and avoiding concentration polarisation. Modern manufacturing techniques such as 3D printing will allow cost-efficient production of three-dimensional shapes. The presented methodology is inherently three-dimensional, and most importantly the computational cost of the adjoint gradient computation is independent of the number of design variables. Hence the presented method will scale-up straightforwardly to more complex three-dimensional spacer optimisation.

Nomenclature

Abbreviations

CFD, computational fluid dynamics
RO, reverse osmosis
SWM, spiral wound membrane
NF, Nano filtration
CP, concentration polarization
AD, automatic differentiation
FD, finite difference

Symbols
$\boldsymbol{u}$, flow velocity vector (m/s)
u, velocity component or magnitude (m/s)
p, static pressure (Pa)
C, solution concentration (kg/m^3)
μ, flow viscosity (Pa·s)
ρ, flow density (kg/m^3)
D, solute diffusion coefficient (m^2/s)
π, osmotic pressure of the solution (Pa)
J_w, water flux (m/s)
K, water permeability coefficient of the membrane

R, observed rejection coefficient
Re, Reynolds number
H, channel height (m)
h, half channel height (m)
L, channel length (m)
J, objective scalar
α, control variable vector
$\boldsymbol{W}$, flow state variables vector
$\boldsymbol{R}$, flow residuals vector
$\boldsymbol{A}$, flow Jacobian matrix
$\boldsymbol{U}$, flow perturbation matrix
$\boldsymbol{v}$, adjoint variable vector

Reference:

[1] Hoekstra AY, Mekonnen MM, Chapagain AK, Mathews RE, Richter BD. Global monthly water scarcity: blue water footprints versus blue water availability. PLoS One. 2012;7:e32688.
[2] Awerbuch L. Future Directions in Integration of Desalination, Energy and the Environment. http://web.mit.edu/ans/www/documents/seminar/S09/awerbuch_slides.pdf>. accessed in 15.09.2015. 2009.
[3] Ahmad AL, Lau KK, Abu Bakar MZ. Impact of different spacer filament geometries on concentration polarization control in narrow membrane channel. Journal of Membrane Science. 2005;262:138-52.
[4] Guillen G, Hoek EMV. Modeling the impacts of feed spacer geometry on reverse osmosis and nanofiltration processes. Chemical Engineering Journal. 2009;149:221-31.
[5] Amokrane M, Sadaoui D, Dudeck M, Koutsou CP. New spacer designs for the performance improvement of the zigzag spacer configuration in spiral-wound membrane modules. Desalination and Water Treatment. 2015:1-9.
[6] Dendukuri D, Karode SK, Kumar A. Flow visualization through spacer filled channels by computational fluid dynamics-II: improved feed spacer designs. Journal of Membrane Science. 2005;249:41-9.
[7] Ranade VV, Kumar A. Fluid dynamics of spacer filled rectangular and curvilinear channels. Journal of Membrane Science. 2006;271:1-15.
[8] Liu J, Liu Z, Liu F, Wei W, Li Z, Wang X, et al. The application of saw-tooth promoter for flat sheet membrane filtration. Desalination. 2015;359:149-55.
[9] Lee J-Y, Tan WS, An J, Chua CK, Tang CY, Fane AG, et al. The potential to enhance membrane module design with 3D printing technology. Journal of Membrane Science. 2016;499:480-90.
[10] Giering R. Tangent linear and adjoint model compiler. User manual, TAMC version. 1997;4.
[11] Oh S, Wang S, Park M, Ha Kim J. Novel Spacer Design Using Topology Optimization in a Reverse Osmosis Channel. Journal of Fluids Engineering. 2013;136:021201--13.
[12] Schwinge J, Wiley DE, Fletcher DF. Simulation of the Flow around Spacer Filaments between Narrow Channel Walls. 1. Hydrodynamics. Industrial & Engineering Chemistry Research. 2002;41:2977-87.
[13] Wardeh S, Morvan H. CFD simulations of flow and concentration polarization in spacer-filled channels for application to water desalination. Chemical Engineering Research and Design. 2008;86:1107-16.
[14] Spiegel E, Veronis G. On the Boussinesq approximation for a compressible fluid. The Astrophysical Journal. 1960;131:442.
[15] Geraldes Vt, Semião V, de Pinho MN. Flow and mass transfer modelling of nanofiltration. Journal of membrane science. 2001;191:109-28.

[16] Gruber M, Johnson C, Tang C, Jensen MH, Yde L, Hélix-Nielsen C. Computational fluid dynamics simulations of flow and concentration polarization in forward osmosis membrane systems. Journal of membrane science. 2011;379:488-95.
[17] Hascoët L. TAPENADE: a tool for Automatic Differentiation of programs. Proceedings of 4th European Congress on Computational Methods, ECCOMAS2004. p. 1-14.
[18] Giering R, Kaminski T. Recipes for adjoint code construction. ACM Transactions on Mathematical Software (TOMS). 1998;24:437-74.
[19] Jones D, Müller J-D, Christakopoulos F. Preparation and assembly of discrete adjoint CFD codes. Computers & Fluids. 2011;46:282-6.
[20] Wright S, Nocedal J. Numerical optimization. Springer Science. 1999;35:7.
[21] Gugala M, Xu S, Müller J-D. Node-based vs. CAD-based approach in CFD adjoint-based shape optimisation. 6th European Conference on Computational Fluid Dynamics2014.
[22] Bird RB, Stewart WE, Lightfoot EN. Transport phenomena. 1960. Madison, USA. 1960.
[23] Berman AS. Laminar flow in channels with porous walls. Journal of Applied physics. 1953;24:1232-5.
[24] Karode SK. Laminar flow in channels with porous walls, revisited. Journal of Membrane Science. 2001;191:237-41.
[25] Fletcher D, Wiley D. A computational fluids dynamics study of buoyancy effects in reverse osmosis. Journal of membrane science. 2004;245:175-81.
[26] Phillip WA, Yong JS, Elimelech M. Reverse draw solute permeation in forward osmosis: modeling and experiments. Environmental science & technology. 2010;44:5170-6.
[27] Hascoet L, Pascual V. The Tapenade Automatic Differentiation tool: principles, model, and specification. ACM Transactions on Mathematical Software (TOMS). 2013;39:20.
[28] Alexiadis A, Wiley DE, Vishnoi A, Lee RHK, Fletcher DF, Bao J. CFD modelling of reverse osmosis membrane flow and validation with experimental results. Desalination. 2007;217:242-50.